Check for updates

Design optimization of mutual dissolution layer and diffusion interface layer in planar heterojunction near-infrared organic phototransistors for ultrahigh photosensitivity

Tao Han, [ID] *[ab] Yimin Zhang,[a] Tianxia Li,[a] Rui Jia,[a] Qingpeng Lai,[a] Bin Li,[a] Suolin Wu,[a] Xianhao Qian,[a] Shufang Ding,[a] Yaqi Chen[a] and Chunzhi Jiang[a]

The interfacial mutual solubility can result in a random distribution of donor and acceptor materials during the spin-coating step in the fabrication of planar heterojunction (PHJ) near-infrared (NIR) organic phototransistors. In this case, deep trap states are induced by acceptors, accelerating electron-hole recombination, ultimately impairing the photoresponsivity of the phototransistor. To solve this issue, a controllable mutual dissolution layer (formed by co-solvent treatment) combined with a diffusion interface layer (formed by the solvent vapor annealing (SVA) method) was introduced to achieve a more ordered arrangement of donors and acceptors, thereby enhancing the electrical performance of PHJ-based NIR phototransistors. Compared with a PDPP3T/PC$_{61}$BM CF device, a PDPP3T/PC$_{61}$BM THF : CF (SVA) device in which the PC$_{61}$BM layer is spin-coated with THF : CF co-solvent and with SVA exhibited a significant performance improvement. The device exhibits a reduction in V_o from 23 V to 4 V, a 5-fold increase in ΔV_{th} (up to ~26.0 V), a 30-fold enhancement in photocurrent (ΔI_{ph} ~64.6 μA), and a dramatic rise in photosensitivity (I_{ph}/I_{dark}) from 205 to 5.6 × 10^8 (850 nm @ 0.1 mW cm^{-2}).

Introduction

Near-infrared (NIR) organic phototransistors hold great potential in flexible wearable electronic devices, especially in medical health monitoring (*e.g.* blood oxygen detection).[1–5] However, the narrow bandgap (~1 eV) of NIR materials facilitates the continuous injection of electrons from the electrodes into the active layer. This results in large dark currents and high turn-on voltages (V_o), which reduce the photoresponse of NIR phototransistors.[6,7] A common approach is to form a bulk heterojunction (BHJ) by incorporating acceptors, which act as electron traps to enhance the photoresponse.[8,9] However, for p-type devices, the introduction of acceptors leads to the formation of trap states. The disordered distribution of donor/acceptor (D/A) phases within the BHJs leads to continuous recombination of holes with electrons during transport, resulting in reduced device performance, such as lower hole mobility.

The issue of photogenerated carrier recombination can theoretically be addressed by employing a planar heterojunction (PHJ) structure in phototransistors.[7,10–15] This is because, on the one hand, the donor layer of PHJ structure can provide a continuous molecular pathway for hole transport, ensuring high device mobility. On the other hand, carriers generated at the p–n interface can exploit the transconductance effect of the phototransistor to enhance the photoresponse. For example, Gao *et al.* developed a novel hybrid-layered phototransistor (C8-BTBT/C8-BTBT:PC$_{61}$BM) with significantly improved photodetection performance. In this device, C8-BTBT served as the conduction channel, C8-BTBT:PC$_{61}$BM acted as the photoactive layer, and a sandwiched MoO$_3$ interlayer functioned as a charge-transport interlayer.[10] Shi *et al.* demonstrated a high-performance bilayer heterojunction phototransistor, where pentacene was utilized as the channel material for photogenerated carrier transport, and ITIC was incorporated to extend the light detection range.[15]

However, the widespread use of lipophilic polymers with similar solubility often leads to interlayer mutual solubility, resulting in the formation of a mutual dissolution interface in PHJ phototransistors.[7,10,16–21] The D:A distribution within the mutual dissolution interface resembles that of BHJs, which impairs carrier transport and degrades device performance. To mitigate the issue of mutual dissolution at the interface, various measures have been explored. For instance, Liu's group employed cross-linked PDPP-DTT to protect the conducting channel of NIR bilayer phototransistors (PDPP-DTT/PDPP-DTT:P$_{61}$BM) from damage during solution processing.[7] Ma's group utilized electrochemical deposition to prepare cross-linked polycarbazole films, addressing the solvent compatibility challenges in the preparation of organic/

[a]Microelectronics and Optoelectronics Technology Key Laboratory of Hunan Higher Education, School of Physics and Electronic Electrical Engineering, Xiangnan University, Chenzhou 423000, P. R. China. E-mail: than@xnu.edu.cn

[b]Hunan Provincial Key Laboratory of Xiangnan Rare-Precious Metals Compounds Research and Application, Xiangnan University, Chenzhou 423000, P. R. China

polymer multilayer devices.[20] In our previous work, a film transfer method (FTM)-based NIR phototransistor was developed, enabling the formation of stable, non-interfering bilayer films that effectively prevent interfacial mutual dissolution.[21]

Although the aforementioned methods are innovative in addressing interfacial mutual solubility challenges, they do not make effective use of spin-coating techniques for organic thin films and have limited applicability. In recent years, the incorporation of mutual dissolution interfaces has been recognized as an effective strategy for enhancing device performance, as demonstrated by its successful application in organic solar cells (OSCs).[22–26] For example, Chen *et al.* employed nanoimprint lithography-assisted sequential blade coating to precisely control donor/acceptor inter-penetration, fabricating high-performance pseudo-planar heterojunction OSCs.[26] This indicates that, with careful control of the mutual dissolution layer, the performance of NIR phototransistors could be improved rather than diminished. Hence, this work innovatively utilizes co-solvent engineering to regulate the mutual dissolution layer. Furthermore, a diffusion interface layer[21] is introduced and combined with the mutual dissolution layer to synergistically optimize the electrical performance of phototransistors. The experimental results and underlying mechanisms are detailed below.

Results and discussion

The devices with different structures are shown in Fig. 1a, S1 and Table 1. As an example, for the PDPP3T/PC$_{61}$BM THF : CF (SVA) device, the PC$_{61}$BM material dissolved in THF : CF co-solvent was spin-coated onto the PDPP3T layer to control the depth of the interfacial dissolution between the PC$_{61}$BM and PDPP3T layers. The bilayer device was then subjected to CF solvent vapor annealing (SVA) at 100 °C. This treatment facilitated the diffusion of the PC$_{61}$BM phase into the PDPP3T layer, forming a diffusion interface layer. Consequently, a device structure with synergistically adjustable mutual dissolution layer and diffusion interface layer was created (Fig. 1a). Based on this design, Fig. 1b schematically illustrates the relationship between the THF : CF co-solvent ratio, mutual dissolution layer thickness, and device photoresponse. Increasing the proportion of the good solvent (CF) enhances the solubility of the bottom film, thereby thickening the mutual dissolution layer. Since device performance is determined by both mutual dissolution layer and diffusion interface layer, an optimal co-solvent ratio is expected to exist that maximizes the photoresponse under a fixed diffusion interface. This hypothesis will be validated through detailed electrical characterization of devices prepared with different co-solvent ratios. Fig. 1c and d present the molecular structures and UV-vis absorption spectra of PDPP3T and PC$_{61}$BM, respectively. It is evident that PDPP3T exhibits a main peak at 850 nm, which is a characteristic feature of near-infrared materials.

Fig. 1e shows the XPS spectra of S 2p elements for different films. The pure PDPP3T film exhibits distinct S 2p$_{3/2}$ and S 2p$_{1/2}$ peaks separated by 1.25 eV, which are consistent with those reported in the literature.[27,28] Peak analysis of other films reveals
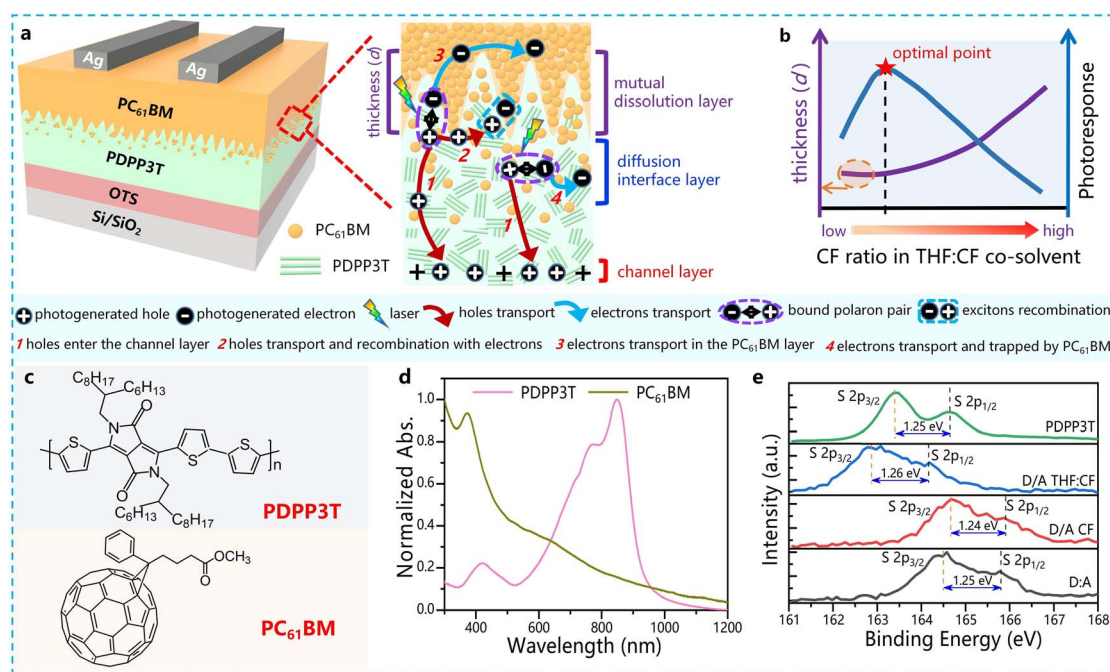
Fig. 1 Device Structure, carriers transport process, schematic of the co-solvent's effect on device, and basic parameters of different films. (a) Device structure, bilayer interface diagram and carriers transport process of PDPP3T/PC$_{61}$BM THF : CF (SVA) device. (b) Schematic of the co-solvent's effect on mutual dissolution layer thickness (*d*) and photoresponse. (c) Molecular structures of PDPP3T and PC$_{61}$BM. (d) UV-vis absorption spectra of PDPP3T and PC$_{61}$BM. (e) XPS spectra of S 2p in different films (D:A represents PDPP3T:PC$_{61}$BM film, D/A CF represents PDPP3T/PC$_{61}$BM CF film, D/A THF : CF represents PDPP3T/PC$_{61}$BM THF : CF film). *d* in the Fig. 1a and b is the thickness of mutual dissolution layer.

Table 1 Device structures with different preparation method[a]

Device	Dielectric layer	First layer	Seceond layer	Electrode
D:A	SiO$_2$ (300 nm)/OTS	PDPP3T:PC$_{61}$BM (transferred)	—	Ag
D/A CF		PDPP3T (transferred)	PC$_{61}$BM (spin-coated with CF solvent)	
D/A THF : CF			PC$_{61}$BM (spin-coated with THF : CF solvent and without SVA)	
D/A THF : CF (SVA)			PC$_{61}$BM (spin-coated with THF : CF solvent and with SVA)	

[a] The thickness of the PDPP3T film and the PDPP3T:PC$_{61}$BM film *via* film transfer method are 110 and 60 nm, respectively.

that PC$_{61}$BM induces varying binding energy shifts in both S 2p$_{3/2}$ and S 2p$_{1/2}$ peaks, with the S 2p$_{1/2}$ peak significantly weakened by PC$_{61}$BM. Notably, for D:A and D/A CF films, the S 2p$_{3/2}$ and S 2p$_{1/2}$ peaks undergo a significant high binding energy shift, indicating that under the influence of the good solvent CF, the donor–acceptor distribution in two films becomes similar. In contrast, the D/A THF : CF film shows a low binding energy shift in the S 2p$_{3/2}$ and S 2p$_{1/2}$ peaks, likely due to partial dissolution of the underlying PDPP3T layer, indicating the formation of a bilayer film distinct from pure PDPP3T and PDPP3T:PC$_{61}$BM film. In addition, literature reported that the thiophene functional groups in PDPP3T possess lone pairs capable of donating electrons.[28,29] On the one hand, in D:A and D/A CF films, the PDPP3T molecular chains are surrounded by numerous dispersed PC$_{61}$BM molecules. Hence, the PDPP3T can readily donate a slight amount of electrons to the PC$_{61}$BM, leading to a shift of the S 2p$_{3/2}$ and S 2p$_{1/2}$ peaks to a higher binding energy (Fig. 1e). On the other hand, for D/A THF : CF films, the structure resembles a quasi-PDPP3T/PC$_{61}$BM bilayer.

Due to the continuity of the PC$_{61}$BM layer and the significant distance between most PDPP3T molecules and the PC$_{61}$BM, PDPP3T tends to receive a slight amount of electrons from the PC$_{61}$BM layer, leading to a shift of the S 2p$_{3/2}$ and S 2p$_{1/2}$ peaks to a lower binding energy (Fig. 1e).

The morphological characterization was conducted to assess the differences between the second PC$_{61}$BM layers prepared with THF : CF and CF solvents (Fig. 2 and S2–5). The absorption spectra of D:A, D/A CF, D/A THF : CF, and D/A THF : CF (SVA) films were characterized (Fig. S2), showing nearly identical peak positions. This confirms that all films consist of the same components—PC$_{61}$BM and PDPP3T—regardless of the film morphology or solvent system used. Fig. S3 and 4 present the surface optical images of different films and device surface photographs with electrodes. The D/A CF bilayer film surface displays a distinct combination of brown and green colors (Fig. S3a). Given that PC$_{61}$BM is a brown powder, it can be inferred that the brown areas on the surface correspond to regions where PC$_{61}$BM phases have aggregated. Furthermore,
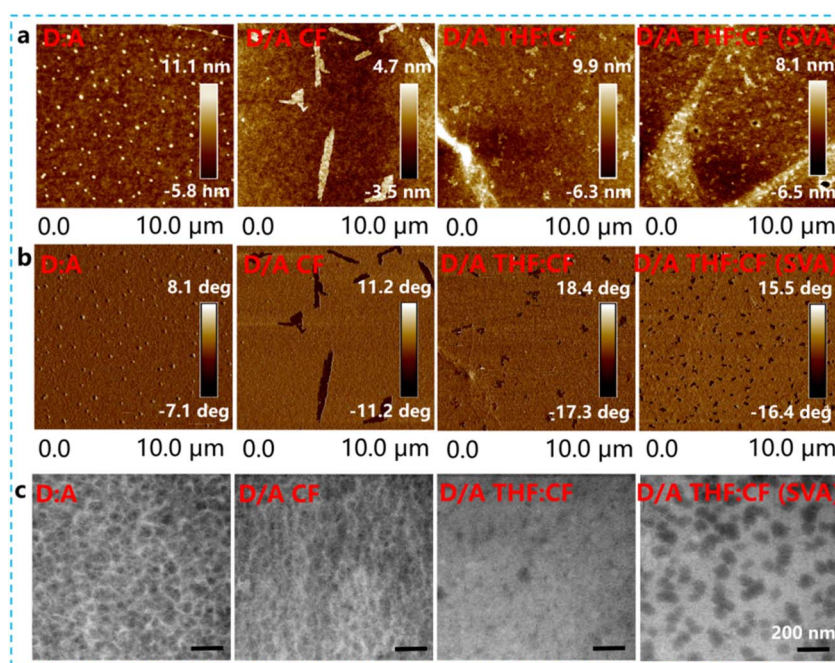

Fig. 2 Morphologies of different films. (a) AFM height images. (b) AFM phase images. (c) TEM. Here, D:A represents PDPP3T:PC$_{61}$BM film, D/A CF represents PDPP3T/PC$_{61}$BM CF film, D/A THF : CF represents PDPP3T/PC$_{61}$BM THF : CF film, D/A THF : CF (SVA) represents PDPP3T/PC$_{61}$BM THF : CF film with SVA treatment.

the surface of the D/A THF : CF bilayer film is more uniform in colour compared to the D/A CF bilayer film due to the limited solubility of THF for the PDPP3T layer. Electrode deposition on films appears uniform, with no noticeable deformation or surface roughness (Fig. S3b). AFM analysis confirms that the surface roughness remains below 10 nm across all samples (Fig. S5), indicating a generally uniform film morphology. Fig. 2a and b present the AFM height and phase images of different films, respectively. Flake-like dark regions are clearly observed in the height image of the D/A CF bilayer film. By correlating with the optical images in Fig. S3a, these flake-like dark regions in the height image can be identified as typical $PC_{61}BM$ aggregation areas. However, only small flake-like areas are observed on the surface of the D/A THF : CF bilayer film when using THF : CF co-solvent. Specifically, $PC_{61}BM$ phases aggregate again when the D/A THF : CF bilayer film undergoes SVA treatment, as shown in Fig. 2b. This is because the small volume of $PC_{61}BM$ facilitates its diffusion during SVA treatment. In this case, part of $PC_{61}BM$ re-aggregates on the surface of $PC_{61}BM$ layer. Meanwhile, another part diffuses into the PDPP3T layer, driven by the concentration gradient, forming a diffusion layer.[21,30]

Fig. 2c and S4b show the TEM morphology of different films. The D:A film exhibits obvious phase separation, with bright areas corresponding to the PDPP3T phase and dark areas to the $PC_{61}BM$ phase.[21,31] However, in the D/A CF bilayer device, the phase separation phenomenon is less pronounced. Furthermore, the D/A THF : CF bilayer film exhibits minimal or no evidence of phase separation. Additionally, TEM images of pure PDPP3T (Fig. S4b) reveal a brighter contrast compared to the D/A THF : CF and D/A THF:CF (SVA) films shown in Fig. 2c. Given that $PC_{61}BM$ typically appears darker in TEM, it can be inferred that the D/A THF:CF film surface is likely covered by a complete $PC_{61}BM$ layer. The results presented earlier suggest that THF : CF co-solvent has a less pronounced erosion effect on the PDPP3T film, leading to insufficient mutual solubility between $PC_{61}BM$ and PDPP3T layer, resulting in minimal phase separation. This will be confirmed through cross-sectional SEM morphology in the following sections. Notably, the D/A THF : CF bilayer film with SVA treatment also shows obvious dark areas, consistent with the AFM morphologies presented (Fig. 2a and b), resulting from $PC_{61}BM$ molecule diffusion/re-aggregation due to their low molecular weight during SVA treatment. For D/A THF : CF bilayer film, the poor solubility of THF is the primary reason preventing phase separation. Additionally, although phase separation can promote charge dissociation in phototransistors, it can also create traps that hinder the transport of holes or electrons.[8,32] Therefore, it is crucial to preserve the integrity of the donor or acceptor layers in the D/A THF : CF phototransistors. This allows photogenerated carriers to be separated at the quasi-planar donor/acceptor interface.[15] Simultaneously, the donor layer facilitates the transport of photogenerated holes, while the acceptor layer enables the separation and storage of electrons. As a result, the photoresponse performance of devices is improved.

The interfacial mutual solubility was studied using cross-sectional SEM images and bilayer interface diagram of the

PDPP3T/$PC_{61}BM$ bilayer films with different solvents, as shown in Fig. 3. Three different solvents were used to dissolve the $PC_{61}BM$ material. For example, the ability of the CF solvent to dissolve the material within the PDPP3T layer makes it difficult to distinguish the boundary between PDPP3T and $PC_{61}BM$ layers, resulting in a large mutual dissolution layer in D/A CF film (Fig. 3a). However, an obvious boundary between PDPP3T and $PC_{61}BM$ layers can be observed in D/A THF : CF film (Fig. 3b). Given that the thickness of a single PDPP3T layer is approximately 110 nm, the reduced thickness of the first PDPP3T layer (∼51.4 nm) in the D/A THF : CF film suggests that it was partially dissolved by the THF : CF co-solvent, which resulted in the formation of a medium-thickness mutual dissolution layer (Fig. 3b).

In addition, a very clear boundary between the bilayers is observed in D/A THF film (Fig. 3c). Additionally, the PDPP3T layer in the D/A THF film is noticeably thicker than in the D/A THF : CF film, indicating that THF solvent has limited solubility for the first PDPP3T layer. This results in a thinner mutual dissolution layer in D/A THF film (Fig. 3c). Based on the SEM morphologies shown in Fig. 3 and device structures in Fig. S1, the thickness of the mutual dissolution layer can be adjusted by optimizing the THF : CF solvent ratio. Based on our previous work, which optimized the diffusion interface through adjustments to the temperature and duration of SVA treatment,[21] the distribution of donors and acceptors in the bilayer film can be precisely controlled. For D/A interface fabrication, solution-processed two-dimensional organic single-crystal heterojunctions have emerged as a promising strategy, enabling high-quality interfaces that effectively suppress trap states and promote efficient charge transport.[33–36] These strategies, however, face significant processing challenges. For instance, Li et al.'s approach necessitates simultaneous interfacial crystallization at solid–liquid and gas–liquid boundaries;[35] Xiao et al.'s two-dimensional phase separation approach relies on blending small-molecule semiconductors with amorphous polymers to achieve high-quality p–n junctions.[36] Our co-solvent/SVA approach enables scalable and reproducible heterojunction fabrication via spin-coating—without requiring crystallization control—making it well-suited for real-world applications.

The electrical properties are subsequently examined to elucidate the impact of mutual dissolution layer and diffusion interface layer on device performance (Fig. 4, S6–12 and Table 2). The transfer curves of different devices without SVA treatment (Fig. 4a) indicate that both the D:A device and the D/A CF device exhibit poor photoresponses. The main reason is that the D/A CF film easily forms an extensive mutual dissolution layer (Fig. 3a), which expands the donor–acceptor mixed region. As shown in the energy level diagram of the device in Fig. S6, photo-generated carriers are expected to dissociate at the PDPP3T/$PC_{61}BM$ interface. Subsequently, holes are transported through PDPP3T and collected by the Ag electrode, while electrons are transferred to $PC_{61}BM$. Assuming negligible effects from film roughness and related factors, Fig. 1a further illustrates the possible charge transport mechanisms influenced by the mutual dissolution layer and the diffusion interface layer.
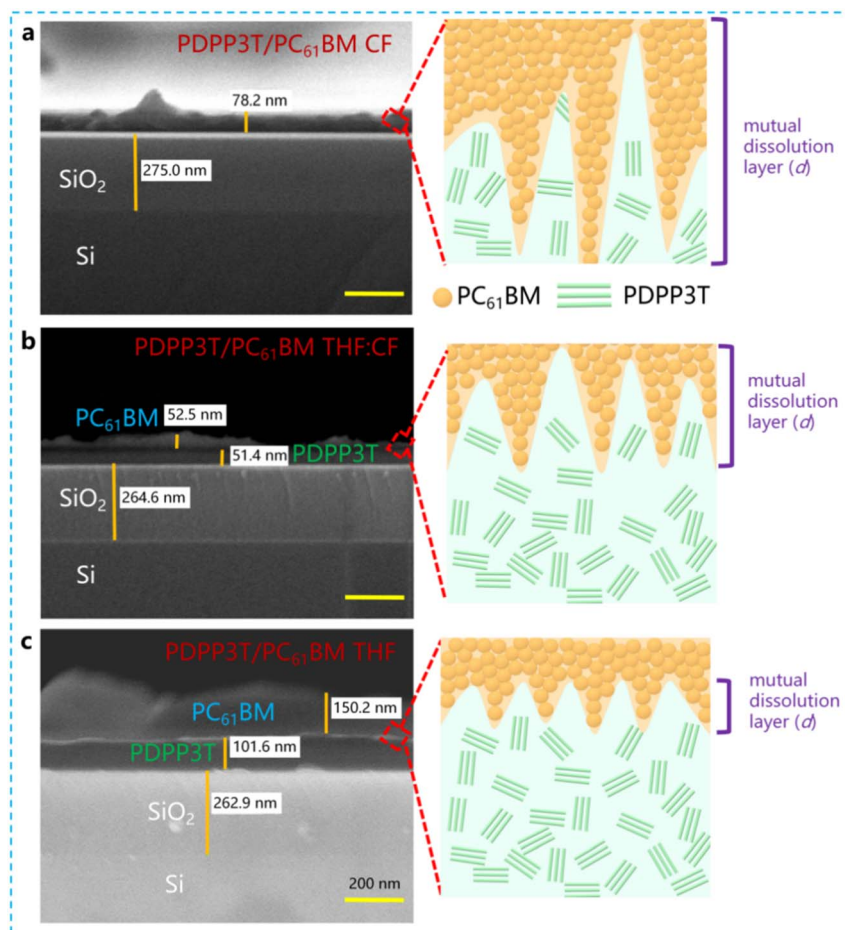
Fig. 3 Cross-sectional SEM images and bilayer interface diagram of different films. (a) PDPP3T/PC$_{61}$BM CF film. (b) PDPP3T/PC$_{61}$BM THF : CF film. (c) PDPP3T/PC$_{61}$BM THF film. d is the thickness of mutual dissolution layer.

For example, in the presence of a large mutual dissolution layer, while exciton generation is enhanced at the donor–acceptor interface, their dissociation competes with recombination due to the high acceptor concentration within the layer. Under illumination, only a small fraction of the photogenerated holes that dissociate at the mutual dissolution interface can enter the conductive channel to increase the photocurrent (path 1, Fig. 1a). Most holes continuously recombine with electrons during transport (path 2, Fig. 1a), leading to poor device photoresponse.[37] This issue can be effectively mitigated by using a THF : CF co-solvent. For example, the D/A THF : CF device demonstrates enhanced photoresponse (Fig. 4a). Combined with Fig. 3b, the optimized mutual dissolution layer reduces the disorder in the donor–acceptor blend. Under light excitation, photogenerated holes are more likely to enter the conductive channel (path 1, Fig. 1a) rather than recombining with electrons at the mutual dissolution interface (path 2, Fig. 1a). Additionally, reducing the mutual dissolution interface facilitates the formation of an acceptor layer, accelerating the transfer of photogenerated electrons (path 3, Fig. 1a) and further decreasing the probability of electron–hole recombination. These findings provide the basis for enhancing the photoresponse of devices. Furthermore, the effectiveness of the SVA

method was evaluated through its application to different devices, as shown in Fig. 4b. The D:A (SVA) device exhibits minimal photoresponse (I_{ph}/I_{dark} ~90), whereas the photoresponse of the D/A CF (SVA) device and the D/A THF : CF (SVA) device shows significant improvement. From the combined observations presented in Fig. 2b, c, and 4b, it can be concluded that diffusion of the PC$_{61}$BM phase occurs during SVA treatment. At the diffusion interface layer, acceptors form a heterojunction with donors, generating extra photogenerated holes that enter the conductive channel, boosting the photocurrent (path 1, Fig. 1a). Conversely, photogenerated electrons are captured by dispersed acceptors,[21,37,38] which do not form continuous electron transport channels (path 4, Fig. 1a). At this point, the photogenerated holes entering the conductive channel will originate from both the mutual dissolution layer and the diffusion interface layer. In other words, the performance enhancement in devices after SVA treatment is attributed to the synergistic effects of the diffusion interface layer and the mutual dissolution layer. For example, in the D/A THF : CF (SVA) device, the photocurrent (ΔI_{ph} ~64.6 μA) is nearly 4-fold that of the D/A THF : CF device (ΔI_{ph} ~16.2 μA) and 30-fold that of the D/A CF device (ΔI_{ph} ~2.1 μA) (0.1 mW cm^{-2} @ 850 nm, Fig. 4c). This suggests that the improvement in the mutual

© 2025 The Author(s). Published by the Royal Society of Chemistry
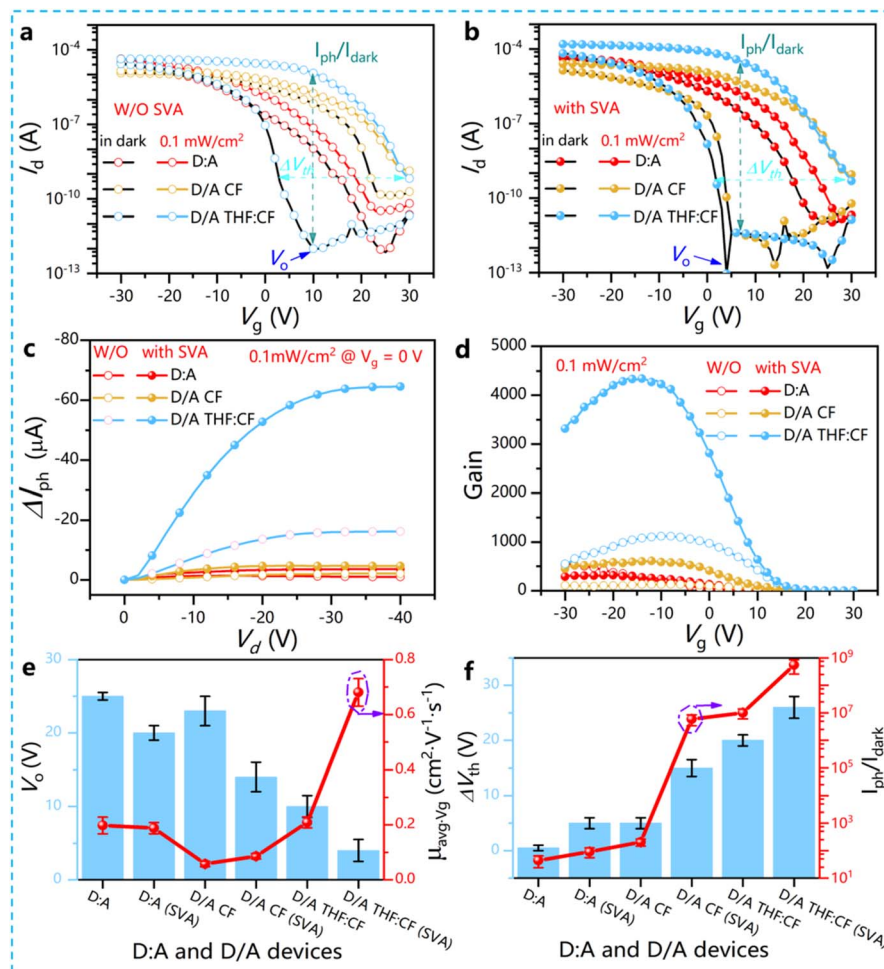
Fig. 4 Electrical properties of D:A and D/A devices. (a) Transfer curves of the devices without SVA. (b) Transfer curves of the devices with SVA. (c) Dependence of ΔI_{ph} on source-drain voltage. (d) Dependence of gain on gate voltage. (e) V_o and $\mu_{avg\ V_g}$. (f) ΔV_{th} and I_{ph}/I_{dark}. The light intensity is shown in Fig. 4a–d and f is 0.1 mW cm^{-2} @ 850 nm. The transfer curves of the devices were measured at a constant $V_d = -30$ V. Here, D:A and D:A (SVA) represent PDPP3T:PC$_{61}$BM film without and with SVA treatment, D/A CF and D/A CF (SVA) represent PDPP3T/PC$_{61}$BM CF film without and with SVA treatment, D/A THF : CF and D/A THF : CF (SVA) represent PDPP3T/PC$_{61}$BM THF : CF film without and with SVA treatment. ΔI_{ph} value is defined as the difference between the saturated photocurrent and the saturated dark current at the same gate voltage in output curves.

Table 2 Performance parameters of different devices[b]

Device	V_o (V) in dark	$\mu_{avg \cdot V_g}$ (cm^2 V^{-1} s^{-1})	ΔV_{th} (V)	I_{ph}/I_{dark}	ΔI_{ph} (µA)	R (A/W) @ $V_g = 0$ V	Gain @ $V_g = 0$ V	D^* (Jones) @ $V_g = 0$ V
PDPP3T:PC$_{61}$BM	25 (±0.5)	0.198 (±0.03)	0.5 (±0.5)	44 (±20)	0.99	28.3	41.3	2.1×10^{12}
PDPP3T:PC$_{61}$BM (SVA)	20 (±1)	0.188 (±0.02)	5 (±1)	90 (±35)	3.6	87	126.9	2.2×10^{12}
PDPP3T/PC$_{61}$BM CF	23 (±2)	0.058 (±0.01)	5 (±1)	205 (±60)	2.1	69.9	102.0	1.4×10^{12}
PDPP3T/PC$_{61}$BM CF (SVA)	14 (±2)	0.086 (±0.01)	15 (±1.5)	5.9×10^6 (±2.5× 10^6)	4.6	273.8	399.4	2.1×10^{13}
PDPP3T/PC$_{61}$BM THF : CF	10 (±1.5)	0.209 (±0.02)	20 (±1)	1×10^7 (±4 × 10^6)	16.2	647.0	943.9	7.6×10^{13}
PDPP3T/PC$_{61}$BM THF : CF (SVA)	4 (±1.5)	0.681 (±0.05)	26 (±2)	5.6×10^8 (±3 × 10^8)	64.6	1876.2	2737.0	5.5×10^{14}

[b] The light intensity is 0.1 mW cm^{-2} @ 850 nm.

dissolution layer accounts for an increase of 14.1 µA in the photocurrent, while the diffusion interface layer contributed an additional 48.4 µA. Correspondingly, the responsivity (R) and gain of the D/A THF : CF (SVA) device reach up to 1876.2 A/W and 2737.0 at $V_g = 0$ V (0.1 mW cm^{-2} @ 850 nm, Fig. 4d, S11b and Table 2), respectively. Notably, the D/A THF : CF (SVA)

device achieves a specific detectivity (D^*) of 5.5×10^{14} Jones at $V_g = 0$ V due to its low dark current and high photocurrent (0.1 mW cm^{-2} @ 850 nm, Fig. S11c). Furthermore, the D/A THF : CF (SVA) device in Fig. S12d exhibits strong photoresponse and high D^* value even under ultralow illumination (e.g., 4 and 20 µW cm^{-2}). Notably, the D^* value reaches ~10^{14} Jones at 4 µW

cm^{-2}, demonstrating exceptional sensitivity and strong potential for real-world scenarios. Additionally, we selected two typical devices, the D:A (SVA) device and the D/A THF : CF (SVA) device, to further analyze the impact of light intensity changes on device performance (Fig. S12). In photoconductive mode (V_g = 20 V), the D/A THF : CF (SVA) device shows a better linear dynamic range (LDR = 61 dB). At the same time, the exponent of the photocurrent increase for this device ($\partial = 0.74$) is higher than that of the D:A (SVA) device ($\partial = 0.4$). More interestingly, with increasing light intensity, the D/A THF : CF (SVA) device shows a stable specific detectivity ($\sim10^{14}$ Jones), far higher than that of the D:A (SVA) device. This highlights its potential for high-sensitivity detection in high-light-intensity scenarios.

In addition, the turn-on voltage (V_o), average hole mobility ($\mu_{avg \cdot V_g}$), turn-on voltage drift (ΔV_{th}), and I_{ph}/I_{dark} of different devices are presented in Fig. 4e and f. It is worth noting that to test the stability of device performance, we selected seven identical samples under each of the different conditions. The experimental errors in Fig. 4e–f and Table 2 show that all devices had good performance reproducibility. Besides, organic films show negligible sensitivity to environmental moisture and oxygen. The first-layer films (e.g., PDPP3T) were fabricated via a solution-transfer method involving spreading the organic solution on deionized water in ambient air, and all electrical measurements were conducted under ambient conditions. Together, these results indicate inherent air stability. Compared to the D:A and D/A CF devices, the D/A THF : CF device in Fig. 4e demonstrates significantly enhanced performance with $\mu_{avg \cdot V_g}$ ~0.209 cm^2 V^{-1} s^{-1}. The degree of interfacial mutual dissolution shown in Fig. 3 indicates that the poor solvent THF effectively shields the p-type conductive channel in the bottom PDPP3T layer from acceptor erosion, thus preserving high hole mobility in the device. This observation indicates that precise control of the mutual dissolution layer is beneficial for improving device performance. Moreover, SVA treatment further enhances the mobility of D/A THF : CF (SVA) devices ($\mu_{avg \cdot V_g}$ ~0.681 cm^2 V^{-1} s^{-1}). We attribute this improvement to part of PC$_{61}$BM re-aggregates induced by thermal annealing (Fig. 2b and c), which reduces hole recombination with stored electrons in the acceptor phase and thereby increases overall charge carrier mobility. Furthermore, Fig. 4e shows that the D/A THF : CF device has a significantly lower turn-on voltage than the D:A and D/A CF devices. As is well known, the narrow bandgap of NIR materials facilitates continuous electrons injection from the electrodes in the dark state, which causes substantial recombination of holes and electrons and leads to a large V_o and a wide hysteresis window.[39] In other words, compared to the pure PDPP3T device (Fig. S7), the randomly distributed acceptor domains in the D:A and D/A CF devices are less effective in blocking electron injection. However, when a well-controlled mutual dissolution layer forms in the D/A THF : CF bilayer device, the acceptor phase becomes more uniformly distributed, facilitating the transfer of injected electrons to the acceptor phase (path 3, Fig. 1a) and consequently reducing V_o of the device. Moreover, the V_o of all devices improved after SVA treatment, indicating that the diffusion interface layer plays a critical role in enhancing phototransistor

performance, likely due to the electron-trapping ability of the formed acceptor (Path 4, Fig. 1a). Fig. 4e and f shows an inverse relationship between ΔV_{th} and V_o: a smaller V_o corresponds to a larger ΔV_{th}. Notably, due to gate-induced suppression of dark current (I_{dark}, Fig. 4b) and enhanced photocurrent via interfacial mutual dissolution and diffusion (Fig. 4c), the D/A THF : CF (SVA) device achieves an excellent I_{ph}/I_{dark} $\sim5.6 \times 10^8$ (Fig. 4f). This I_{ph}/I_{dark} value surpasses that of most state-of-the-art organic phototransistors,[7–9,40,41] highlighting its exceptional photoresponse capability.

Given the improvement effects of mutual dissolution layer and diffusion interface layer on device performance, different THF : CF co-solvent ratios, solvents and organic bilayer film systems were selected to adjust electrical properties (Fig. 5, S9–10, and S13–19). Fig. 5a and S15a show that the electrical performance of SVA-treated devices varies to different extents with changes in the THF : CF ratio. After optimization, the bilayer device achieves the lowest V_o value, the highest mobility, and the largest ΔV_{th} and I_{ph}/I_{dark} values when using the THF : CF (7 : 3) co-solvent. Fig. 3 shows that varying the THF : CF ratio alters the thickness of the mutual dissolution interface, indicating a strong correlation between interface thickness and device performance. This supports the relationship proposed in Fig. 1b among co-solvent ratio, mutual dissolution layer thickness, and photoresponse. Besides, when the second PC$_{61}$BM layers were spin-coated using co-solvents (THF : CF, THF : CB, and THF : DCB), the devices showed significantly reduced V_o and improved ΔV_{th} and I_{ph}/I_{dark} compared to those using single solvents (e.g., CF, CB, and DCB) in Fig. 5b and S15b. Furthermore, the hole mobility of devices using THF : CF as the solvent was higher than that of devices using CF solvent (Fig. S15b). These results indicate that the mutual dissolution layer can be engineered through the use of multiple solvent systems. Notably, although THF and CF deliver excellent processing performance, they present notable drawbacks: THF is flammable and potentially toxic upon long-term exposure, while CF is highly toxic and environmentally persistent. To address these issues, we will systematically explore greener solvents in future work to improve the sustainability and industrial viability of this technology.

Furthermore, other organic bilayer systems were selected to demonstrate the generality of device performance modulation via synergistic mutual dissolution layer and diffusion interface layer, as shown in Fig. 5c and S19. PC$_{71}$BM and L8-BO[42] were selected as acceptors, while DPPT-TT[43] and IDT-BT[44] were used as donors, with their molecular structures and UV-vis absorption spectra provided (Fig. S16). The IDT-BT (absorption peaks: 668 nm and 415 nm) has relatively narrow bandgap (1.7 eV) facilitates electron injection from the electrode into the active layer,[45] resulting in a large V_o and electrical performance similar to near-infrared materials. Therefore, a 405 nm wavelength light source was selected to excite the IDT-BT/PC$_{61}$BM (CF or THF : CF) bilayer device. Notably, all the PDPP3T/PC$_{61}$BM, IDT-BT/ PC$_{61}$BM, DPPT-TT/PC$_{61}$BM, PDPP3T/PC$_{71}$BM, and PDPP3T/L8-BO devices exhibited improved performance after the application of the THF : CF co-solvent and SVA treatment. These observations confirm that the synergistic effect of the mutual
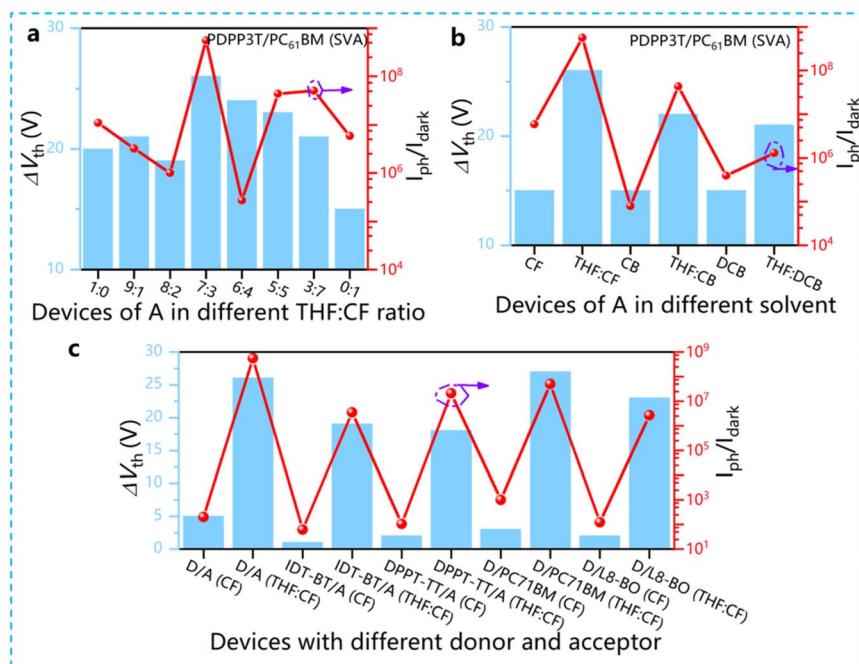
Fig. 5 Regulation of the solvent type, THF : CF co-solvent ratio and organic bilayer film systems to adjust electrical properties. (a) ΔV_{th} and I_{ph}/I_{dark} of PDPP3T:PC$_{61}$BM devices with PC$_{61}$BM dissolved in different THF : CF co-solvent ratio after SVA treatment. (b) ΔV_{th} and I_{ph}/I_{dark} of PDPP3T:PC$_{61}$BM devices with PC$_{61}$BM dissolved in different solvent after SVA treatment. (c) ΔV_{th} and I_{ph}/I_{dark} of devices with different donor and acceptor. Here, D/A (CF or THF : CF), IDT-BT/A (CF or THF : CF), DPPT-TT/A (CF or THF : CF), D/PC$_{71}$BM (CF or THF : CF) and D/L8-BO (CF or THF : CF) represent PDPP3T/PC$_{61}$BM (CF or THF : CF), IDT-BT/PC$_{61}$BM (CF or THF : CF), DPPT-TT/PC$_{61}$BM (CF or THF : CF), PDPP3T/PC$_{71}$BM (CF or THF : CF) and PDPP3T/L8-BO (CF or THF : CF) devices, respectively. In addition, all the ratio of THF : CF, THF : CB, and THF : DCB co-solvent in Fig. 5b and c is 7 : 3. The devices with CF and THF : CF solvent are treated without SVA and SVA in Fig. 5c, respectively. The light intensity is 0.1 mW cm^{-2} @ 850 nm except IDT-BT/PC$_{61}$BM (CF or THF : CF) device (the light intensity is 0.05 mW cm^{-2} @ 405 nm).

dissolution layer and diffusion interface layer also contributes to the enhancement of performance in other organic bilayer film systems. This finding provides valuable insights for the design and the development of new types of bilayer phototransistors.

Conlusions

This research demonstrates the preparation of high-performance PHJ-based NIR phototransistors by achieving precise control over donor and acceptor distribution. This was accomplished through the systematic optimization of the mutual dissolution layer and diffusion interface layer. The resulting PDPP3T/PC$_{61}$BM THF : CF (SVA) phototransistor achieved an ultrahigh R value of 1876.2 A/W, gain value of 2737.0 at $V_g = 0$ V, and I_{ph}/I_{dark} value of 5.6×10^8 (850 nm @ 0.1 mW cm^{-2}). Due to the well-controlled distribution of acceptors, electrons injected from the electrodes in the dark state were efficiently captured, resulting in a small turn-on voltage of 4 V and a large turn-on voltage shift of 26 V. Performance improvements were observed in bilayer systems across various solvent type and different donor–acceptor combinations, demonstrating the broad applicability of the synergistic enhancement effect of the mutual dissolution layer and the diffusion interface layer. This strategy provides a viable pathway for the development of high-performance bilayer phototransistors.

Experimental

Materials

Octadecyltrichlorosilane (OTS, 98%), dichlorobenzene (DCB, 99.9%), and chlorobenzene (CB, 99.9%) were purchased from J & K Scientific. CHCl$_3$ (CF, 99.8%) was obtained from Sigma-Aldrich. Poly[[2,3,5,6-tetrahydro-2,5-bis(2-hexyloctyl)-3,6-dioxopyrrolo[3,4-*c*]pyrrole-1,4-diyl][2,2′; 5′,2″-terthiophene]-5,5″-diyl] (PDPP3T), Poly[[4,4,9,9-tetrahexadecyl-4,9-dihydro-*s*-indaceno [1,2-*b*:5,6-*b*′]dithiophene-2,7-diyl)-*alt*-(benzo[*c*][1,2,5] thiadiazole-4,7-diyl) (IDT-BT), poly(3,6-di(2-thien-5-yl)-2,5-di(2-octyldodecyl)-pyrrolo[3,4-*c*]pyrrole-1,4-dione)thieno[3,2-*b*]thiophene) (DPPT-TT), (6,6)-phenyl C71 butyric acid methyl ester, mixture of isomers (PC$_{71}$BM) and 2,2′-((2*Z*,2′*Z*)-((12,13-bis(2-ethylhexyl)-3,9-(2-butyloctyl)-12,13-dihydro-[1,2,5]thiadiazolo[3,4-*e*]thieno[2″,3″:4′,5′]thieno[2′,3′:4,5]pyrrolo[3,2-*g*]thieno[2′,3′:4,5] thieno[3,2-*b*]indole-2,10-diyl)bis(methanylylidene))bis(5,6-difluoro-3-oxo-2,3-dihydro-1*H*-indene-2,1-diylidene))dimalononitrile (L8-BO) were sourced from Solarmer Materials. (6,6)-Phenyl C61 butyric acid methyl ester (PC$_{61}$BM) was bought from 1-Material. High n-doped silicon (Si) with a 300 nm thermally grown SiO$_2$ layer was used as the substrate.

Device fabrication

The Si/SiO$_2$ substrate and a boat containing OTS (30 μL) were placed in a Petri dish covered with aluminum foil, and then

heated on a hot plate in a nitrogen atmosphere (140 °C, 12 hours) to prepare the OTS self-assembled monolayer. Excess OTS was removed by spin-coating CF onto the Si/SiO$_2$ substrate. PDPP3T solution (0.25 wt%), PDPP3T : PC$_{61}$BM solution (0.2 wt%, D/A ratio = 1 : 1), DPPT-TT solution (0.25 wt%), and IDT-BT solution (0.25 wt%) were dissolved in a CF/CB co-solvent (volume ratio = 10 : 1). All solutions were stirred at 100 °C for more than 12 hours. PDPP3T, PDPP3T:PC$_{61}$BM, DPPT-TT, and IDT-BT layers were prepared on the Si/SiO$_2$/OTS substrate using the FTM, as described in our previous work.[21,33] For example, a 110 nm thick PDPP3T layer was obtained by dropping 50 μL of PDPP3T solution into deionized water at 10 °C using the FTM. All FTM-based film preparations were carried out in a vacuum for 20 minutes, followed by annealing at 100 °C for 10 minutes to enhance film crystallinity.

PC$_{61}$BM (0.2 wt%) was dissolved in a THF : CF co-solvent (volume ratio = 10 : 0–0 : 10), DCB : CF (volume ratios = 0 : 10 and 7 : 3), and CB : CF (volume ratios = 0 : 10 and 7 : 3). The solution was spin-coated (2000 rpm, 60 s) onto the PDPP3T layer, the DPPT-TT layer, and the IDT-BT layer to form the PC$_{61}$BM layer. L8-BO (0.2 wt%), and PC$_{71}$BM (0.2 wt%) were dissolved in THF : CF (volume ratios = 0 : 10 and 7 : 3) and spin-coated (2000 rpm, 60 s) onto the PDPP3T layer to prepare the L8-BO, and PC$_{71}$BM layers. During all spin-coating processes, the second layer film was prepared by quickly dropping 50 μL of solution onto a rotating substrate. This approach minimized the dissolution of the first layer by the solvent of the second layer. For bilayer film devices requiring SVA treatment, the devices were first placed in a Petri dish containing 30 μL of CF, then covered with aluminum foil, and annealed at 100 °C for 30 minutes in a nitrogen glove box.

Phototransistor characterization

Absorption spectroscopy (UV-vis) was carried out using a UV-3100 spectrophotometer (Shimadzu). Thin film thickness was measured with a Dektak 150 instrument (Veeco). Atomic force microscopy (AFM) was performed using a Dimension Edge instrument (Bruker). X-ray photoelectron spectroscopy (XPS) data were collected on a Nexsa (Thermo Fisher) system. Transmission electron microscopy (TEM) images were acquired using a JEOL-2100F instrument (JEOL). Scanning electron microscopy (SEM) were obtained using a Sigma 300 instrument (Zeiss). Film surface optical images were captured using a IVTEST-1200 optical microscope instrument (IVTEST). Devices surface photographs with electrodes were obtained using a Canon EOS 850D instrument. The electrical performance of the phototransistors was characterized in an air atmosphere using a four-terminal semiconductor parameter analyzer (Keithley 2636B). The light illumination was provided by an Opolette 355 LDinstrument (Opotek) with 850 nm and a diodepumped crystal laser (Newport CL-2000) with 405 nm.

Calculation formulae

The device mobility (μ) in the saturation regime was determined using the following equation:[46]

$$\mu = \frac{2L}{WC_i}\left(\frac{\partial\sqrt{I_d}}{\partial V_g}\right)^2 \tag{1}$$

where the channel length L is 40 μm, and the channel width W is 1000 μm and the dielectric capacitance per unit area C_i is 11.5 nF cm^{-2}. Here, I_d denotes the drain current, and V_g corresponds to the gate voltage.

The average mobility ($\mu_{avg \cdot V_g}$) was calculated from the average slope of the saturation transfer curves.[47]

Furthermore, the responsivity (R), gain (G), Specific detectivity (D^*) and linear dynamic range (LDR) were determined as follows:[21,48]

$$R = \frac{\Delta I_{Ph}}{P_{inc}} \tag{2}$$

$$G = R \times \frac{1240(nm\ W\ A^{-1})}{\lambda} \tag{3}$$

$$D^* = \frac{R \times \sqrt{A}}{\sqrt{2q \cdot I_{dark}}} \tag{4}$$

$$LDR = 20\log\frac{L_{upper}}{L_{lower}}(dB) \tag{5}$$

where ΔI_{ph} indicates the photocurrent in ampere, P_{inc} refers to the incident light power in watt, λ represents the wavelength of the incident light in nanometer, A is the device conductive channel area ($A = L \times W = 1 \times 10^{-4}$ cm^2), I_{dark} is dark current, L_{upper} and L_{lower} are the maximum and minimum detectable light intensity in linear range.

Author contributions

T. H. conceived the idea and oversaw the project. Y. Z., T. L., and R. J. assembled the devices and assessed their electrical properties. Y. Z. and T. L. captured the film surface optical images and performed SEM analysis. Q. L., B. L., and S. W. conducted TEM and AFM measurements. X. Q., S. D. and Y. C. carried out the XPS testing. S. D. and C. J. outlined the mechanism of the mutual dissolution layer and diffusion interface layer. T. H. analyzed the results and drafted the manuscript.

Conflicts of interest

There are no conflicts to declare.

Data availability

The data supporting this article have been included as part of the SI (*e.g.* structure of different devices, UV-vis absorption, morphologies of films, AFM, energy level diagram and electrical properties of devices). See DOI: **https://doi.org/10.1039/d5ra05574a**.

Acknowledgements

Notes and references

1 S. Alam, S. Sim, M. Q. Li, S. Yang, J. Lee and J. Lee, *Mater. Today Chem.*, 2025, **46**, 102718.

2 K. Zhang, J. Wu, C. Sun, D. S. Chung, Y. Geng and L. Ye, *Nat. Rev. Mater.*, 2025, **10**, 487.

3 Y. Tang, Z. Wang, M. Gao, J. Han, L. Yuan and F. Zhu, *Nat. Commun.*, 2025, **16**, 7144.

4 Z. Yu, H. Chen, R. Han, H. Qin, Z. Yao, H. Liu, Y. Ma, X. Wan, G. Li and Y. Chen, *Natl. Sci. Rev.*, 2024, **11**, nwad311.

5 X. Zhao, J. Wang, M. Liu, X. Ma and F. Zhang, *Adv. Opt. Mater.*, 2024, **12**, 2401087.

6 D. Zhu, D. Ji, L. Li and W. Hu, *J. Mater. Chem. C*, 2022, **10**, 13312.

7 Q. Li, Y. Ran, W. Shi, M. Qin, Y. Sun, J. Kuang, H. Wang, H. Chen, Y. Guo and Y. Liu, *Appl. Mater. Today*, 2021, **22**, 100899.

8 G. Baroni, F. Reginato, S. Mattiello, S. Moschetto, M. Prosa, M. Bolognesi, L. Beverina and S. Toffanin, *ACS Appl. Electron. Mater.*, 2025, **7**, 3694.

9 L. Zhao, H. Xie, J. Xia and Y. Hu, *Appl. Phys. Lett.*, 2024, **124**, 243301.

10 Y. Gao, Y. Yi, X. Wang, H. Meng, D. Lei, X. Yu, P. K. Chu and J. Li, *Adv. Mater.*, 2019, **31**, 1900763.

11 H. Kim, Z. Wu, N. Eedugurala, J. D. Azoulay and T. N. Ng, *ACS Appl. Mater. Interfaces*, 2019, **11**, 36880.

12 D.-H. Lim, M. Kang, S.-Y. Jang, K. Hwang, I.-B. Kim, E. Jung, Y.-R. Jo, Y.-J. Kim, J. Kim, H. Choi, T. Kim, S. Mathur, B.-J. Kim and D.-Y. Kim, *ACS Appl. Mater. Interfaces*, 2020, **12**, 25066.

13 F. Huang, X. Wang, K. Xu, Y. Liang, Y. Peng and G. Liu, *J. Mater. Chem. C*, 2018, **6**, 8804.

14 J. Han, J. Wang, M. Yang, X. Kong, X. Chen, Z. Huang, H. Guo, J. Gou, S. Tao, Z. Liu, Z. Wu, Y. Jiang and X. Wang, *Adv. Mater.*, 2018, **30**, 1804020.

15 K. Shi, R. Jin, S. Huang, H. Lei, P. Dai, D. Chi, W. Zhang and G. Yu, *J. Mater. Chem. C*, 2021, **9**, 322.

16 X. Li, X. Du, J. Zhao, H. Lin, C. Zheng and S. Tao, *Sol. RRL*, 2021, **5**, 2000592.

17 M. Ren, G. Zhang, Z. Chen, J. Xiao, X. Jiao, Y. Zou, H.-L. Yip and Y. Cao, *ACS Appl. Mater. Interfaces*, 2020, **12**, 13077.

18 Z. Zhong, L. Bu, P. Zhu, T. Xiao, B. Fan, L. Ying, G. Lu, G. Yu, F. Huang and Y. Cao, *ACS Appl. Mater. Interfaces*, 2019, **11**, 8350.

19 A. Pierre, A. Gaikwad and A. C. Arias, *Nat. Photonics*, 2017, **11**, 193.

20 J. Qi, Y. Gao, X. Zhou, D. Yang, W. Qiao, D. Ma and Z. Y. Wang, *Adv. Mater. Interfaces*, 2015, **2**, 1400475.

21 T. Han, Z. Wang, N. Shen, Z. Zhou, X. Hou, S. Ding, C. Jiang, X. Huang, X. Zhang and L. Liu, *Nat. Commun.*, 2022, **13**, 1332.

22 D. Li, A. M. Kay, D. B. Riley, O. J. Sandberg, A. Armin and P. Meredith, *Adv. Energy Mater.*, 2025, **15**, 2500816.

23 Z. Zhao, S. Chung, L. Tan, J. Zhao, Y. Liu, X. Li, L. Bai, H. Lee, M. Jeong, K. Cho and Z. Kan, *Energy Environ. Sci.*, 2025, **18**, 2791.

24 H. Wang, B. Zhang, L. Wang, X. Guo, L. Mei, B. Cheng, W. Sun, L. Kan, X. Xia, X. Hao, T. Geue, F. Liu, M. Zhang and X.-K. Chen, *Angew. Chem. Int. Edit.*, 2025, **137**, e202508257.

25 S. Gao, S. Xu, C. Sun, L. Yu, J. Li, R. Li, X. Liu, X. Zhou, H. Chen, Y. Lin, X. Bao, W. Zhu and X. Song, *Adv. Mater.*, 2025, **37**, 2420631.

26 H. Mao, J. Zhang, X. Cen, J. Zhang, L. Wen, J. Xue, D. Luo, L. Zhang, Z. Qin, W. Ma, L. Tan and Y. Chen, *Energy Environ. Sci.*, 2024, **17**, 6799.

27 H. Yoo, M. Ghittorelli, D.-K. Lee, E. C. P. Smits, G. H. Gelinck, H. Ahn, H.-K. Lee, F. Torricelli and J.-J. Kim, *Sci. Rep.*, 2017, **7**, 5015.

28 P. Chen, X. Ma, Z. Wang, N. Yang, J. Luo, K. Chen, P. Liu, W. Xie and Q. Hu, *Phys. Chem. Chem. Phys.*, 2024, **26**, 14874.

29 R. Wadhwa, D. Kaur, Y. Zhang, A. Alexander, D. Kumar, P. Kumar, M. A. G. Namboothiry, Q. Qiao and M. Kumar, *Appl. Surf. Sci.*, 2023, **632**, 157597.

30 D. Chen, F. Liu, C. Wang, A. Nakahara and T. P. Russell, *Nano Lett.*, 2011, **11**, 2071.

31 T. Han, S. Zhou, Y. Chen, Q. Du, Y. Li, Y. Mo, B. Li, S. Ding, Y. Chen and C. Jiang, *ACS Appl. Mater. Interfaces*, 2023, **15**, 50321.

32 T. Han, L. Sun, Q. Feng, K. Cao, S. Ding, G. Jin, C. Jiang and X. Huang, *J. Mater. Chem. C*, 2020, **8**, 12284.

33 X. Tian, J. Yao, L. Zhang, B. Han, J. Shi, J. Su, J. Liu, C. Li, X. Liu, T. Zhai and L. Jiang, *Nano Res.*, 2022, **15**, 2667.

34 Y. Du, Q. Sun, Y. Ren, L. Sun, Y. Xie, X. Wu, M. Zhang, H. Zhang, H. Cheng, R. Ding and J. Feng, *Adv. Mater. Technol.*, 2025, **10**, 2500495.

35 H. Li, J. Wu, K. Takahashi, J. Ren, R. Wu, H. Cai, J. Wang, H. L. Xin, Q. Miao, H. Yamada, H. Chen and H. Li, *J. Am. Chem. Soc.*, 2019, **141**, 10007.

36 M. Xiao, J. Liu, C. Liu, G. Han, Y. Shi, C. Li, X. Zhang, Y. Hu, Z. Liu, X. Gao, Z. Cai, J. Liu, Y. Yi, S. Wang, D. Wang, W. Hu, Y. Liu, H. Sirringhaus and L. Jiang, *Nat. Commun.*, 2021, **12**, 2774.

37 L. Qin, L. Wu, B. Kattel, C. Li, Y. Zhang, Y. Hou, J. Wu and W.-L. Chan, *Adv. Funct. Mater.*, 2017, **27**, 1704173.

38 L. Li, F. Zhang, W. Wang, Q. An, J. Wang, Q. Sun and M. Zhang, *ACS Appl. Mater. Interfaces*, 2015, **7**, 5890.

39 B. Park, S. Choi, S. Graham and E. Reichmanis, *J. Phys. Chem. C*, 2012, **116**, 9390.

40 F. Ling, Y. Zhang, Q. Du, X. Zheng, Q. Liu, W. Wang and S. Qin, *J. Mater. Chem. C*, 2024, **12**, 16131.

41 R. Shyam, P. K. Aich, U. Pandey, B. N. Pal and R. Prakash, *IEEE Sens. J.*, 2024, **24**, 32004.

42 C. He, Y. Pan, Y. Ouyang, Q. Shen, Y. Gao, K. Yan, J. Fang, Y. Chen, C.-Q. Ma, J. Min, C. Zhang, L. Zuo and H. Chen, *Energy Environ. Sci.*, 2022, **15**, 2537.

43 H. Wei, P.-A. Chen, J. Guo, Y. Liu, X. Qiu, H. Chen, Z. Zeng, T.-Q. Nguyen and Y. Hu, *Adv. Funct. Mater.*, 2021, **31**, 2102768.

44 A. Wadsworth, H. Chen, K. J. Thorley, C. Cendra, M. Nikolka, H. Bristow, M. Moser, A. Salleo, T. D. Anthopoulos, H. Sirringhaus and I. McCulloch, *J. Am. Chem. Soc.*, 2019, **142**, 652.

45 M. Xiao, A. Sadhanala, M. Abdi-Jalebi, T. H. Thomas, X. Ren, T. Zhang, H. Chen, R. L. Carey, Q. Wang, S. P. Senanayak, C. Jellett, A. Onwubiko, M. Moser, H. Liao, W. Yue, I. McCulloch, M. Nikolka and H. Sirringhaus, *Adv. Funct. Mater.*, 2021, **31**, 2007359.

46 H. H. Choi, K. Cho, C. D. Frisbie, H. Sirringhaus and V. Podzorov, *Nat. Mater.*, 2018, **17**, 2.

47 Z. Wang, H. Guo, J. Li, L. Wang and G. Dong, *Adv. Mater. Interfaces*, 2019, **6**, 1801736.

48 J. Huang, J. Lee, J. Vollbrecht, V. V. Brus, A. L. Dixon, D. X. Cao, Z. Zhu, Z. Du, H. Wang, K. Cho, G. C. Bazan and T.-Q. Nguyen, *Adv. Mater.*, 2020, **32**, 1906027.